Weierstraß-Institut
für Angewandte Analysis und Stochastik
Leibniz-Institut im Forschungsverbund Berlin e. V.

Preprint ISSN 2198-5855

The impact of microcavity wire width on polariton soliton existence and multistability

Gabriela Slavcheva[1], Mirella V. Koleva[2], Alexander Pimenov[3]

submitted: March 28, 2017

[1] Department of Physics
University of Bath
Bath, BA2 7AY
United Kingdom
E-Mail: g.slavcheva@bath.ac.uk

[2] Department of Physics
University of Oxford
Oxford, OX1 3RH
United Kingdom
E-Mail: mirella.koleva@physics.ox.ac.uk

[3] Weierstrass Institute
Mohrenstr. 39
10117 Berlin
Germany
E-Mail: alexander.pimenov@wias-berlin.de

No. 2381
Berlin 2017

2010 *Physics and Astronomy Classification Scheme.* 05.45.-a, 42.65.Pc, 42.65.Tg.

Key words and phrases. Polaritons, solitons, microcavities, multi-stability, tilted waveguides.

The authors wish to thank A. V. Gorbach and D. V. Skryabin for helpful discussions. G.S. acknowledges funding through the Leverhulme Trust Research Project Grant No. RPG-2012-481. A. P. acknowledges support from SFB 787 of the DFG.

Edited by
Weierstraß-Institut für Angewandte Analysis und Stochastik (WIAS)
Leibniz-Institut im Forschungsverbund Berlin e. V.
Mohrenstraße 39
10117 Berlin
Germany

Fax: +49 30 20372-303
E-Mail: preprint@wias-berlin.de
World Wide Web: http://www.wias-berlin.de/

The impact of microcavity wire width on polariton soliton existence and multistability

Gabriela Slavcheva, Mirella V. Koleva, Alexander Pimenov

Abstract

We have developed a model of the nonlinear polariton dynamics in realistic 3D non-planar microcavity wires in the driven-dissipative regime [15]. We find that the typical microcavity optical bistability evolves into multi-stability upon variation of the model parameters. The origin of the multi-stability is discussed in detail. We apply linear perturbation analysis to modulational instabilities, and identify conditions for localisation of composite multi-mode polariton solitons in the triggered parametric oscillator regime. Further, we demonstrate stable polariton soliton propagation in tilted and tapered waveguides, and determine maximum tilt angles for which solitons are still found. Additionally, we study soliton amplitude and velocity dependence on the wire width, with a view towards device applications.

1 Introduction

Semiconductor quantum-well (QW) microcavities are 1D photonic crystal structures, specifically designed to control light-matter interactions. The strong coupling emitter-cavity regime of operation is realised when the QW exciton-cavity photon interaction exceeds any dissipative rates in the system. The eigenmodes of the system are mixed, entangled light-matter states that can be viewed as photons 'dressed' with the medium polarisation (exciton); these give rise to bosonic quasiparticles known as microcavity exciton-polaritons. Owing to their photon component, exciton-polaritons are extremely light particles. Due to their excitonic component, however, they exhibit strong repulsive inter-particle interactions, resulting in strong nonlinearities, nearly four orders of magnitude higher than in typical nonlinear solid-state optical media [1]. The nonlinearities arise primarily from parametric scattering of exciton-polaritons, driven by a Coulomb exchange interaction between polariton excitonic constituents, with additional smaller contributions originating from phase space filling [2–4].

Nonlinear self-localisation and coherent propagation phenomena with exciton polaritons in planar microcavities have been extensively studied in recent years. Formation of moving 2D self-localised, non-equilibrium polariton droplets travelling without loss at high speeds ($\sim 1\%$ of the speed of light) has been experimentally demonstrated in coherently pumped semiconductor microcavities operating in the strong-coupling regime [5]. These polaritons display collective dynamics consistent with superfluidity. When studying polariton flow around a defect, it has been demonstrated that at high flow velocities, the perturbation induced by the defect gives rise to the turbulent emission of quantised vortices and to the nucleation of oblique, dark 'quantum hydrodynamic' solitons [6]. Accurate tracking in space and time of long-life ($100 - 200$ ps) polaritons reveals long-range ballistic propagation and coherent flow over macroscopic distances – from hundreds of μm to millimetres within the cavity [7–9].

It is well known that a high density and low temperature gas of microcavity polaritons exhibits effects pertinent to cold-atom Bose-Einstein condensates [10]. However, unlike atomic condensates, for which bright solitons exist only for attractive interactions, while repulsive interactions give rise to dark solitons,

DOI 10.20347/WIAS.PREPRINT.2381 Berlin 2017

bright polariton solitons supported by repulsive exciton-exciton interactions have been theoretically predicted [11] and experimentally demonstrated [12] for pump momenta beyond the inflection point of the lower polariton branch, where the polariton effective mass becomes negative. Self-localisation (in a direction collinear with the pump wave vector) occurs when the dispersion induced by the negative polariton effective mass compensates the repulsive polariton-polariton interaction. Coherent polariton propagation has also been experimentally demonstrated in laterally confined microcavity wires, fabricated by lateral etching of planar semiconductor microcavities [13]. Condensed polaritons spread over the whole wire, with the higher-energy excitons remaining at the excitation spot [14].

Polariton waves can be confined into structures with sub-μm size. This opens up possibilities for fabrication of polaritonic integrated circuits based on structured semiconductor microcavities on a chip. Polaritonic structured media are currently under active development, with arrays of microcavity wires currently being fabricated to act as waveguides for polariton waves. Structured microcavities are a particularly promising integration platform, due to the large polaritonic nonlinearity, broad transparency window, mature fabrication technology and the possibility of monolithic integration with semiconductor diode lasers and VCSELs. In this respect, new theories and numerical methods are needed to model the nonlinear polariton dynamics in non-planar waveguides.

We have recently developed a driven-dissipative, scalar (spinless) Gross-Pitaveskii model of the nonlinear polariton dynamics in realistic microcavity wires. In addition, we have numerically demonstrated multimode polariton solitons and a peculiar type of spatial multistability [15]. Under suitable conditions, different modes within the polariton soliton wave packet interact among themselves in such a way as to give rise to a self-localisation mechanism that prevents the pulse from broadening. Self-localisation phenomena in multimode systems arise due to counter-balancing nonlinearity with a combination of dispersive effects: material (polariton) dispersion due to frequency-dependent dielectric response, cavity modes dispersion, and variation of the group velocity of each mode. In a recent work [16], using the coupled-mode expansion technique we showed that a new component of the nonlinearity has to be taken into account, namely the intermodal nonlinear coupling. The latter arises from two distinct nonlinear phenomena: intermodal cross-phase modulation (through Kerr nonlinearity) and degenerate four-wave mixing (through polariton parametric scattering).

In this work, we provide more details of our general mean-field, driven-dissipative Gross-Pitaevskii model. We apply it to the problem of polariton soliton propagation in microcavity wires with different widths – with a view to designing integrated polaritonic devices. Using the model, we study the soliton existence domain, multistability and group velocity dependence on the wire width, and identify optimum geometry parameters for soliton formation. We provide a qualitative explanation of the non-monotonic dependence of the soliton branches and group velocity dependence on the wire width. Additionally, we investigate the dependence of the multistability on the cavity-emitter system's dissipation parameter, which includes exciton reservoir dephasing and cavity photon decay. Furthermore, we demonstrate numerically a new coherent propagation phenomenon of a radiating polariton soliton exhibiting periodic collapses and revivals, and identify regimes for existence of this new class polariton solitons in a realistic microcavity wire. Finally, we simulate polariton soliton propagation in tilted and tapered microcavity wires, and determine the maximum tilt angle for which the soliton persists.

2 Theoretical model

We consider a microcavity polariton wire, fabricated by laterally etching a planar GaAs/AlGaAs microcavity, of the type described in [13]. The corresponding geometry is schematically shown in Fig.

1 (a). The wire is pumped by a CW laser linearly polarised in the y direction, such that it supports quasi-TE modes in the wire. The pump is inclined along the x direction at an angle θ, contained within the x-z plane, so that it has a non-zero momentum along the wire. Similar to the case of a planar microcavity [12], solitons propagating along the wire are triggered by a short seed pulse also incident at θ, having the same linear polarisation as the CW pump. We describe the dynamics of the system by a scalar mean-field driven-dissipative Gross-Pitaevskii model [15]:

$$\begin{aligned} \partial_t E - i\left(\partial_x^2 + \partial_y^2\right) E + \left[\gamma_c - i\delta_c - i\Delta - iU(y)\right] E = i\Omega_R(y)\Psi + E_p e^{i\kappa x} \ , \\ \partial_t \Psi + \left(\gamma_e - i\delta_e - i\Delta\right)\Psi + i\left|\Psi\right|^2\Psi = i\Omega_R(y)E \ , \end{aligned} \tag{1}$$

where E_p is the normalized pump amplitude, g is the strength of exciton-exciton interaction [12], ω_R is the Rabi frequency in a planar homogeneous cavity, time is measured in units of $T = 1/\omega_R$, and E and Ψ are the averages of the photon and exciton creation or annihilation operators. The normalisation is such that $(\omega_R/g)|E|^2$ and $(\omega_R/g)|\Psi|^2$ are the photon and exciton numbers per unit area. The unit length, $L = \sqrt{\hbar/(2m_c\omega_R)}$, is determined by the effective cavity photon mass, m_c. δ_e, δ_c, and the pump frequency, Δ, are detunings from a reference frequency, $\hbar\omega_0 = 1.55$ eV ($\lambda_0 = 800$ nm), normalised with respect to the Rabi frequency. γ_c and γ_e are cavity and exciton decay rates. The lateral confinement in the cavity plane (along the y axis) is described by an effective potential $U(y)$ in the photonic component and a spatially confined normalised coupling $\Omega_R(y)$:

$$U(y) = U_{bg}\left[1 - e^{-(2y/w)^8}\right] \ , \ \Omega_R(y) = e^{-(2y/w)^8} \ , \tag{2}$$

where w is the dimensionless wire width and U_{bg} is the background confinement potential. As demonstrated in our previous work [15], the above super-Gaussian potentials give an accurate description of the dispersion of the lowest six guided modes of the wire, which includes the fundamental mode.

3 Numerical results

3.1 Free-polariton modes dispersion and model parameters

The free-polariton dispersion is calculated from our mean-field model (Eqs. (1) and (1)). By setting $E_p = 0$ in Eq. (1) and neglecting the nonlinear term in Eq. (1), using the ansatz $E = A(y)e^{i\kappa x - i\omega t}$, $\Psi = B(y)e^{i\kappa x - i\omega t}$, the dispersion of the linear modes, $\omega(\kappa)$, is given by the following eigenvalue problem:

$$\kappa^2 A = \left[\omega + \delta_c + U - \frac{\Omega_R^2}{\omega + \delta_e + i\gamma_e} + \partial_y^2 - i\gamma_c\right] A \ . \tag{3}$$

The resulting linear polariton dispersion for the fundamental and the next 5 modes is shown in Fig. 1 (b), along with the single-mode planar microcavity dispersion (black solid lines) for a microcavity wire width of $3\ \mu$m and a pump tilt angle of 20° at zero pump detuning, $\Delta = 0$. The planar microcavity can be regarded as a limiting case of a microcavity wire when the width, $w \to \infty$. Thus, it is clear from the figure that, for the pump energy that we are using (just above the lower polariton branch (blue-detuned from the LP resonance frequency)), the planar microcavity dispersion in the reciprocal momentum space is steeper than that of the microcavity wire. The real part of the corresponding linear E-field and Ψ-field fundamental and higher-order mode profiles are shown in Fig. 1 (c) and (d), respectively.

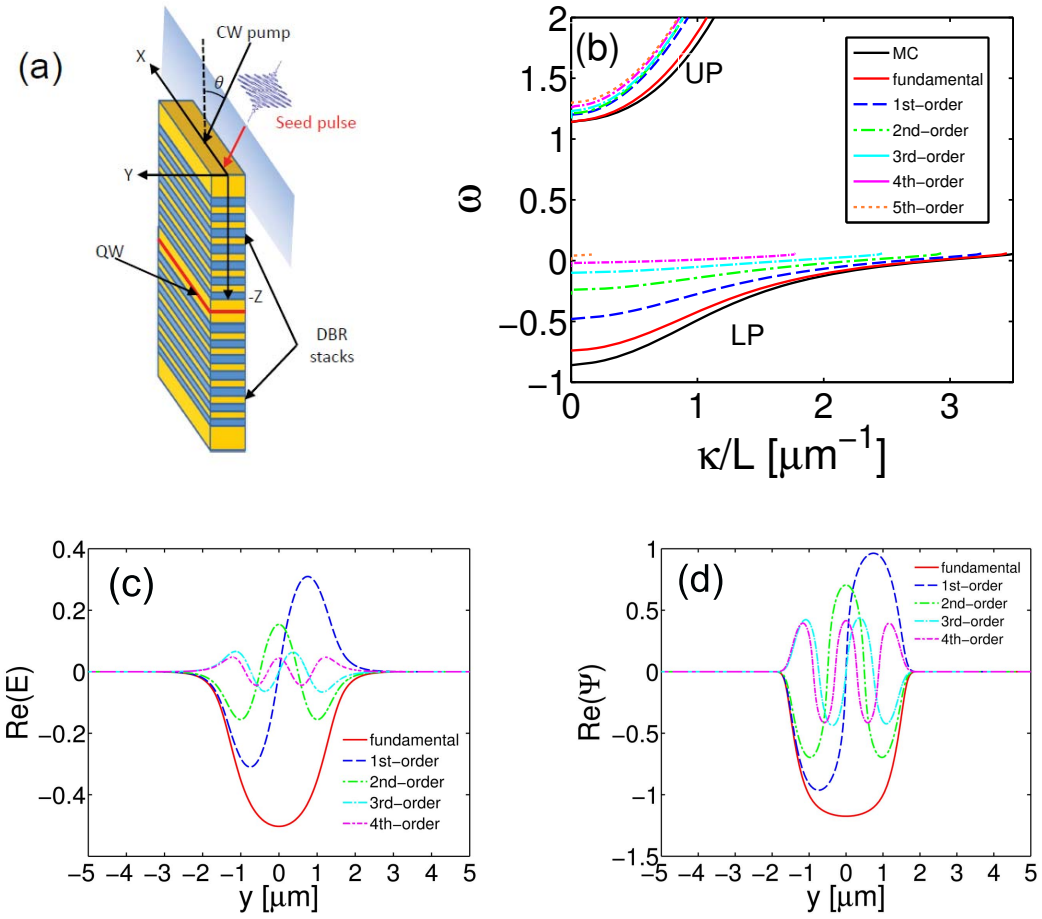

Figure 1: (Color online) (a) Scheme of the microcavity polaritonic wire structure and the excitation geometry. The CW pump and the seed pulse are incident along the x direction at an angle of incidence θ, and have no components in the y direction; (b) Linear polariton dispersion (ω is a dimensionless frequency) for the fundamental and next five higher-order modes at zero detuning, $\Delta = 0$, wire width $w = 3\ \mu\mathrm{m}$ and a pump incidence angle $\theta = 20^{\circ}$. Both the lower (LP) and upper (UP) polariton branches are shown. The planar microcavity dispersion is displayed with solid black lines for comparison. Amplitudes of the corresponding (c) linear photonic (E) electric field modes and (d) excitonic (Ψ) field modes.

The model free parameters, namely the Rabi frequency ω_R, the spatial scale L, and the effective potential depth U_{bg} are obtained by fitting the free-polariton dispersion with the numerically computed dispersion of a realistic microcavity wire structure, using the finite-element Maxwell solver, COMSOL, as described in [15].

For the chosen value of the normalised quantum-well oscillator strength, $H = 0.015$, the Rabi splitting in the fundamental mode is $2\hbar\omega_R \approx 11\ \mathrm{meV}$ at normal incidence ($\kappa = 0$), thus comparable to the one in planar cavities. Using this value, the model parameters in Eqs. (1) and (1) are: $T_0 \approx 0.12$ ps, $\delta_c = -0.191$, $\delta_e = -0.1$, and $\gamma_c = \gamma_e = 0.04$, corresponding to exciton and cavity linewidths, $\Gamma_e = \Gamma_c = 0.22\ \mathrm{meV}$ [12].

3.2 Stationary nonlinear modes

The stationary solutions of the nonlinear system, Eqs. (1) and (1), in the presence of a spatially homogeneous monochromatic pump, are obtained by setting all time derivatives to zero, restoring the pump and the nonlinearity, and seeking stationary solutions to the homogeneous system of the form $\{E, \Psi\} = \{A(y)\, e^{i\kappa x}, B(y)\, e^{i\kappa x}\}$. The system then reduces to:

$$\begin{aligned} \left[\delta_c + \Delta + U - \kappa^2 + \partial_y^2 + i\gamma_c\right] A + \Omega_R B = iE_p\ , \\ \left(\delta_e + \Delta + i\gamma_e\right) B - |B|^2 B + \Omega_R A = 0\ . \end{aligned} \tag{4}$$

After discretising the y co-ordinate, this system transforms into a set of coupled nonlinear algebraic equations, which is solved numerically for E and Ψ, e.g. using Newton-Raphson iterations for each fixed set of pump parameters E_p and κ.

All calculations are carried out for a microcavity polaritonic wire of width $w = 3\,\mu\mathrm{m}$ at a pump incidence angle $\theta = 20^\circ$. In what follows, we choose to plot the Ψ-field power, $\int |\Psi|^2 dy$, integrated in a transverse direction to the channel, in order to avoid any spurious non-monotonic behaviour which arises if the maximum or the channel midpoint value of $|E|^2$ or $|\Psi|^2$ are plotted.

The integrated power of the Ψ-field is plotted at zero pump amplitude, $E_p = 0$, and no dissipation, $\gamma_e = \gamma_c = 0$ for different Δ. The number of confined modes for the specific potential considered is 6 (including the fundamental mode), corresponding to the family of curves displayed in Fig. 2 (a). Scanning through a range of pump amplitudes shows that a bi- or multi-stability family of curves, shown in Fig. 2 (b, d), is obtained for a range of dissipation dimensionless parameters, γ. We start with $\gamma = 0.04$ (corresponding to $\Gamma_e = \Gamma_c = 0.22\,\mathrm{meV}$), which is the most realistic value [12], and decrease γ towards the limiting case of zero dissipation, $\gamma = 0$. Each point of the multistability curve corresponds to a polariton (E, Ψ) mode. The curve in (d) clearly exhibits three distinct branches and two loops, as opposed to the commonly found single bistability loop observed in (b).

The multiple loops found is a new result specific to the 1D microcavity wires, and is markedly distinct from the simple bistability observed in planar microcavities. Here below we analyse the origin of the multi-stability.

The bistability curves for $\Delta = -0.1$, parameterised using γ, are plotted in Fig. 2 (b). These clearly exhibit a single loop. In this case, only the first two (fundamental and first-order) modes of the family could be excited (see left vertical dashed line in (a) intersecting two modes). However, since the pump is spatially symmetric, the first-order mode does not arise, and therefore the fundamental polariton mode, shown in Fig. 2 (c), is observed in both the lower and upper bistability branches in Fig. 2 (b)

– including at the bifurcation point (denoted '1'). The bifurcation point heralds the appearance of an additional stable state.

At $\Delta = 0$, with $w = 3\,\mu\mathrm{m}$ and model parameters as set out at the end of Sec. 3.1, four modes could be excited (see right vertical line in (a), intersecting four nonlinear modes). Note that, due to the even parity of the pump, only even modes survive – i.e. the fundamental and second order. The dependence of the excitonic-field power, $\int |\Psi|^2 dy$, on the pump amplitude exhibits multistability (two loops and two left-folding points), see Fig. 2 (d). For both detunings considered, the bi- and multistability behaviour becomes increasingly pronounced as the dissipation is reduced. Note that the two leftmost turning points in (d) touch the ordinate at $\gamma = 0$. The real and imaginary parts of the modes corresponding to each turning point are plotted in Fig. 2 (e) and (f). By comparing (d) with the intersection points in (a) for $\Delta = 0$, one can clearly see that the leftmost bifurcation points, denoted by '2' and '3' in Fig. 2 (d), correspond to a second-order and a fundamental mode, respectively.

As we show above, the predicted multistability is an interplay between the symmetric Gaussian pump and the number of modes supported by the microcavity wire potential. The latter can be controlled by selecting the confinement potential depth (U_{bg}) and width (w).

3.3 Modulational Instability

Once a stationary mode $\{A, B\}$ is found, we can analyze its stability by introducing a small perturbation:

$$E = A(y) + \alpha[\epsilon_f(y)e^{iqx - i\delta t + \lambda t} + \epsilon_b^*(y)e^{-iqx + i\delta t + \lambda t}]e^{i\kappa x}\,, \tag{5}$$

$$\Psi = B(y) + \alpha[p_f(y)e^{iqx - i\delta t + \lambda t} + p_b^*(y)e^{-iqx + i\delta t + \lambda t}]e^{i\kappa x}\,, \tag{6}$$

where δ and λ are real, α is a scaling parameter, q is the perturbation wave vector, and the subscripts f and b stand for 'forward' and 'backward'-propagating waves, respectively.

Assuming small amplitude perturbations $\varepsilon_{f,b}$ and $p_{f,b}$, neglecting the second-order terms $O\left(\varepsilon_{f,b}^2\right)$ and $O\left(p_{f,b}^2\right)$ and introducing $\vec{x} = [\epsilon_f, \epsilon_b, p_f, p_b]^T$, the system can be recast as the eigenvalue problem:

$$(\delta + i\lambda)\vec{x} = \hat{M}\vec{x}\,, \qquad \hat{M} = \begin{bmatrix} -\mathcal{L}_f & 0 & -\Omega_R & 0 \\ 0 & \mathcal{L}_b^* & 0 & \Omega_R \\ -\Omega_R & 0 & -\mathcal{P} & B^2 \\ 0 & \Omega_R & -(B^*)^2 & \mathcal{P}^* \end{bmatrix}\,, \tag{7}$$

$$\mathcal{L}_{f,b} = \partial_y^2 - (\kappa \pm q)^2 + \delta_c + \Delta + U + i\gamma_c, \quad \mathcal{P} = \delta_e + \Delta - 2|B|^2 + i\gamma_e\,. \tag{8}$$

We find the eigenvectors, $\vec{x}$, and the complex eigenvalues ($\delta + i\lambda$) of the large sparse $4N \times 4M$ matrix, $\hat{M}$, each matrix element of which is a $N \times M$ block matrix, N and M being the number of grid points along the x and y directions (typically, $N = M = 2048$). We then plot the maximum of the eigenvalues' imaginary part, λ, against a small range of values of the q wave vector, choosing $\Delta = 0$. We designate the names 'branch 1', 'branch 2' and 'branch 3' within the curves shown in Fig. 2 (d) for the consecutive sections with a positive gradient, starting to count from the bottom of the graph. Typical full eigenvalue spectra for all three branches in Fig. 2 (d) are shown in Fig. 3.

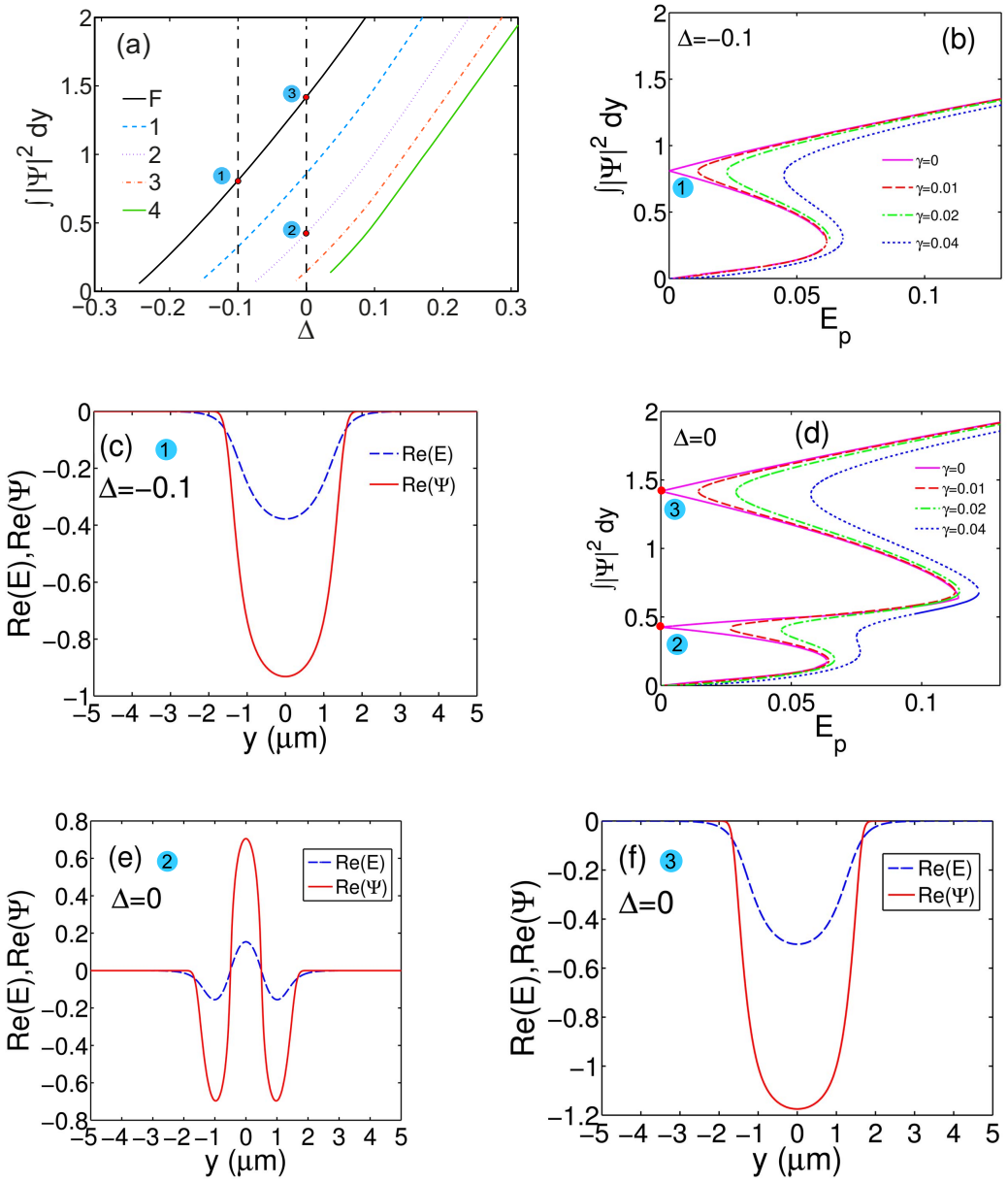

Figure 2: (Color online) (a) Integrated power of the excitonic (Ψ) electric field at pump amplitude $E_p = 0$ and $\gamma_c = \gamma_e = 0$ for five nonlinear modes (F, fundamental; 1, first order; 2, second order; 3, third order; 4, fourth order) as a function of Δ, the detuning from the reference pump frequency, ω_0. Vertical dashed lines help to determine which modes are present for different detunings. (b) Ψ-field power as a function of E_p for different dissipation parameters, $\gamma_e = \gamma_c = \gamma$, and $\Delta = -0.1$. A bistability curve is observed. Note that we take the pump to be spatially symmetric. The single folding point 1 corresponds to the fundamental (even) mode (see panel (a) and text for more details). (c) Cross-sectional profile of the real parts of the photonic (E) electric field and Ψ-field of the fundamental polariton mode, corresponding to the single folding point, denoted '1', in (b). (d) Ψ-field power as a function of E_p for different dissipation parameters, $\gamma_e = \gamma_c = \gamma$, and $\Delta = 0$. A multistability curve is observed. The multistability arises from the fact that, for this detuning, two rather than one polaritonic modes are supported (see panel (a) and text for more details). The multistability curve touches the y axis at two folding points, 2 and 3. The bi- and multistability in (b) and (d) becomes more pronounced as γ is decreased, from 0.04 to 0. (e, f) Real part of the E-field and Ψ-field of the nonlinear polariton mode profiles at $\Delta = 0$ at the two folding points 2 and 3 in (d), respectively. Folding point 2 corresponds to a second-order mode, while point 3 corresponds to a fundamental mode.

DOI 10.20347/WIAS.PREPRINT.2381 Berlin 2017

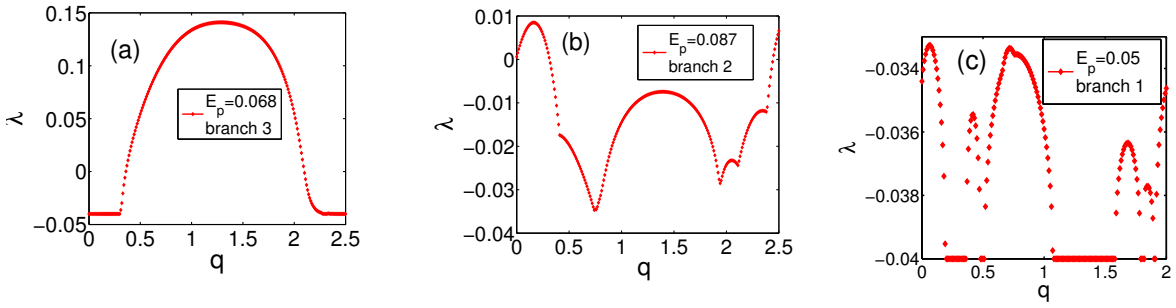

Figure 3: (Color online) Maximum imaginary part (λ) of the eigenvalue spectrum of the matrix $\hat{M}$, as a function of the perturbation wave vector, q, for a stationary nonlinear solution belonging to different parts of the multistability curve. If branches 1 (lower), 2 (middle) and 3 (top) signify consecutive sections of the curve with positive slope, beginning to count from the abscissa, then the results shown on this figure are representative of (a) branch 3 at pump amplitude, $E_p = 0.068$; (b) branch 2 at $E_p = 0.087$; (c) branch 1 at $E_p = 0.05$. $\Delta = 0$ everywhere.

In Fig. 4 (a), we plot the equivalent of the multistability curve from Fig. 2 (d) at $\gamma = 0.04$ for the integrated E-field power as a function of pump amplitude, E_p. The stability of each point on the curve is analysed by the following method. If, for a given E_p, the relevant curve in Fig. 3 contains at least one point for which $\lambda > 0$ (as long as it is not the one at $q = 0$), then the corresponding point on the multistability curve is deemed to be 'modulationally unstable'. By inspection of Fig. 3 (a), this is the case for branch 3, and the manifold of all such points is coloured in green in Fig. 4 (a). This type of instability may lead to the formation of stable localised entities, such as solitons. If, on the other hand, the curve lies below zero, the corresponding point on the multistability curve is classified as stable (such as is the case for branch 1). If the curve lies entirely above zero (or if at least $\lambda(q = 0) > 0$), the corresponding point is classified as 'unstable' (branch 2). The modes (real and imaginary parts of the E- and Ψ-fields), corresponding to each of the multistability curve branches, are shown in Fig. 4 (b), bottom row.

To verify the above linear stability analysis, we perform a dynamical check by solving Eq.(1–1) in the time domain by the split-step method, propagating the perturbed mode at $E_p = 0.068$ and $q = 1.2$ in Fig. 3(a). Snapshots at $t = 0.4$ and $20\,\mathrm{ps}$ of the time evolution of the perturbed solution are shown in Fig. 5 (a) and (b), respectively, for a mode at $E_p = 0.068$, lying on the third branch (see Fig. 4 (a)) and for an eigenvalue corresponding to the aforementioned q value. In agreement with the stability analysis above, this perturbed solution is modulationally unstable and exhibits localisation and soliton-like features at later times (Fig. 5 (b)). By contrast, the snapshots at $t = 0.4$ and $28.4\,\mathrm{ps}$, shown in Fig. 6 (a) and (b), respectively, correspond to a perturbed solution at $E_p = 0.087$, lying on the second branch at $q = 0.2$ (Fig. 3 (b)), which is unstable. In this case, the time evolution exhibits filamentation, rather than localisation and soliton-like features.

The magenta curve above the third (topmost) branch in Fig. 4 (a) is the soliton branch. It is represented by the integrated E-field power along the transverse cross-section through the soliton maximum, which was computed by the 2D Newton method. The shaded area indicates the region in which solitons exist.

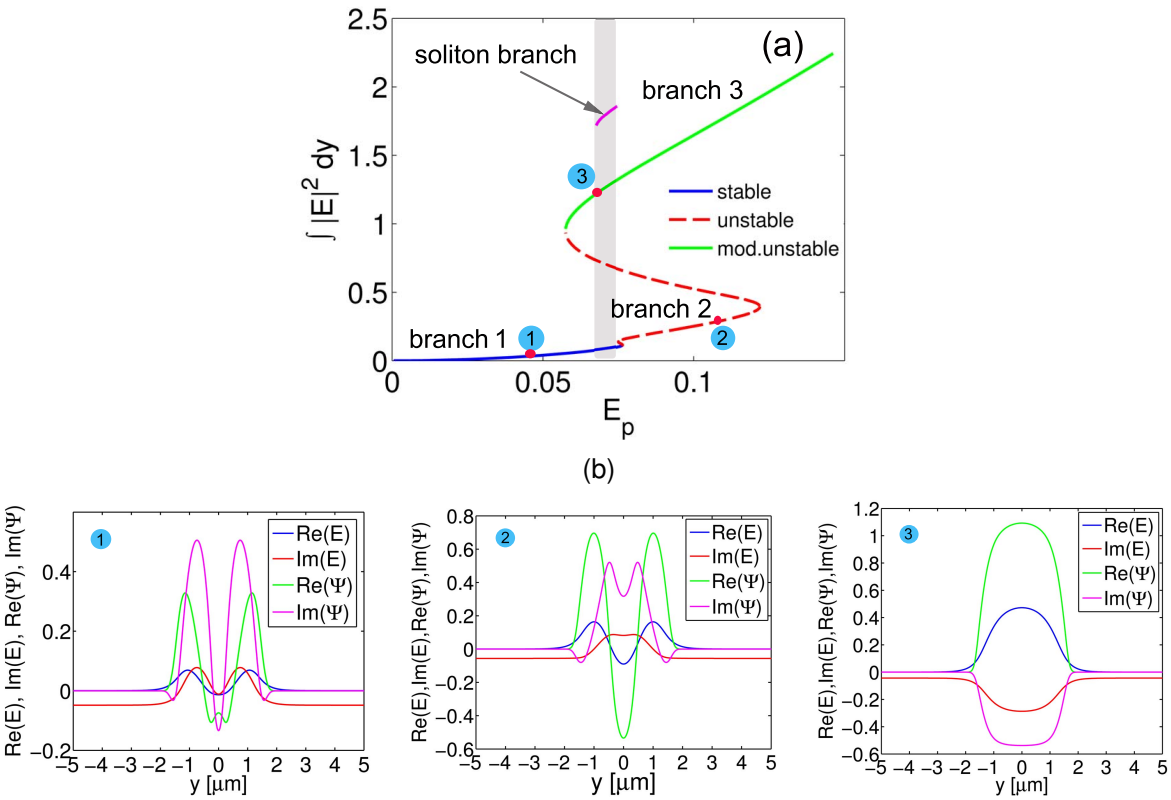

Figure 4: (Color online) (a) Multistability curve of the power of the photon's electric field (E), integrated along the y direction, as a function of pump amplitude, E_p, at $\gamma = 0.04$ and $\Delta = 0$ for the stationary solutions of a microcavity polaritonic wire with waveguide width $w = 3\,\mu\mathrm{m}$ at a pump incidence angle $\theta = 20°$. Each point on the curve corresponds to a specific polariton mode, shown in (b) (bottom row of this figure). Three distinct branches are discernible, depending on the type of solution obtained: stable (blue), modulationally unstable (green), and unstable (dashed red) solutions. The curve in magenta above the topmost branch represents the soliton branch, and was calculated numerically by the 2D Newton method. The shaded area indicates the region in which solitons exist. (b) Real and imaginary parts of the nonlinear photon (E) and exciton (Ψ) field modes at the points indicated in (a). Note that: we have a fourth-order mode at point 1 (on branch 1); a second-order mode at point 2 (on branch 2); a fundamental mode at point 3 (on branch 3).

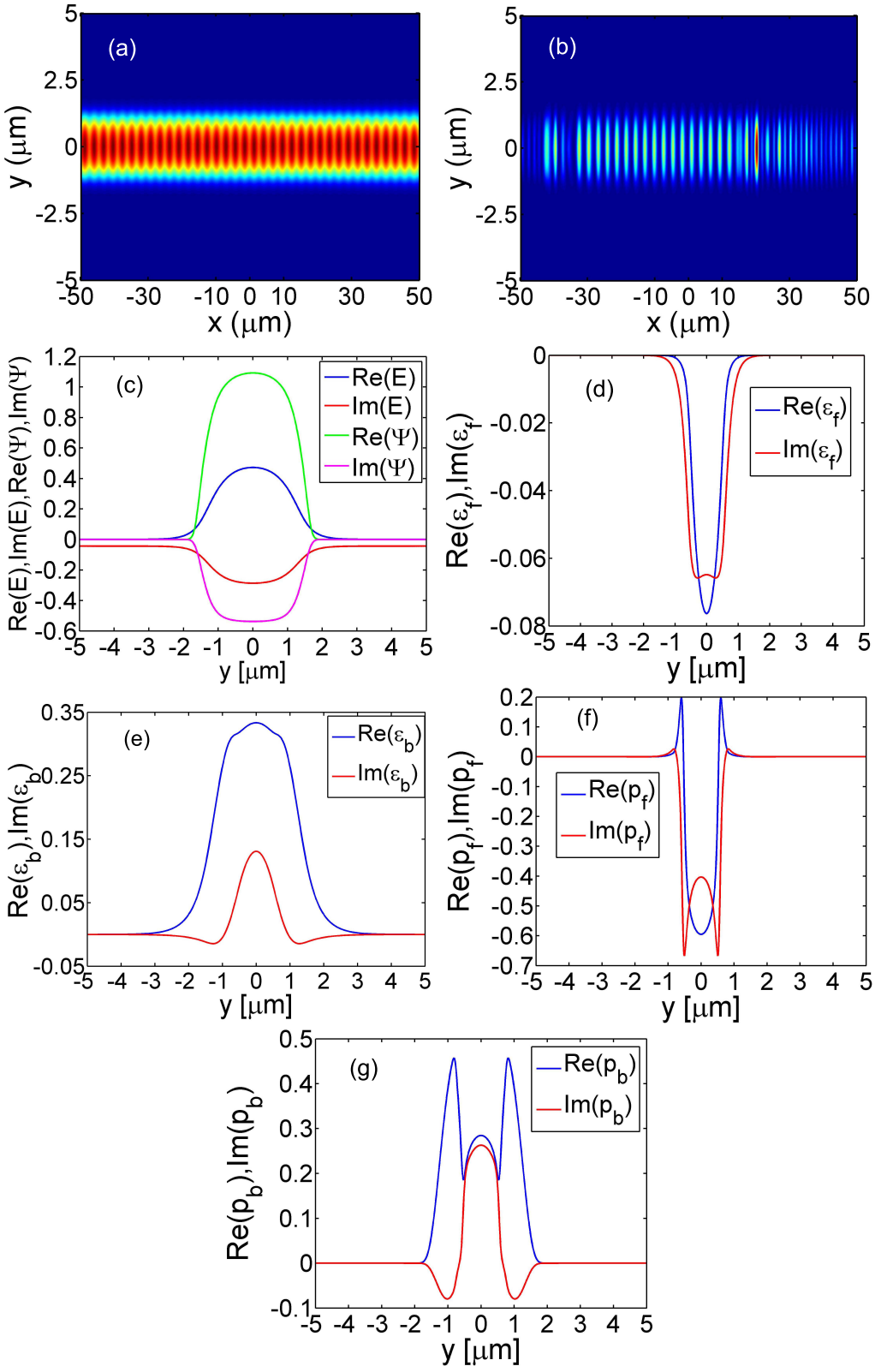

Figure 5: (Color online) Dynamical check of the modulational instability of the stationary solution: snapshots of the time evolution of the perturbed mode power at pump amplitude $E_p = 0.068$ and perturbation wave vector $q = 1.2$ (corresponding to the third branch, see Fig. 4 (a), and Fig. 3 (a)) at (a) $t = 0.4\,\mathrm{ps}$ and (b) $t = 20\,\mathrm{ps}$. Clearly, the modulational instability on the third branch leads to localisation and concomitant formation of a soliton. (c) Real and imaginary parts of the nonlinear polariton mode of the photon (E) and exciton (Ψ) for $E_p = 0.068$, which is on the third branch. (d–g) Real and imaginary parts of the perturbation eigenvectors, computed from Eq. 7.

DOI 10.20347/WIAS.PREPRINT.2381 Berlin 2017

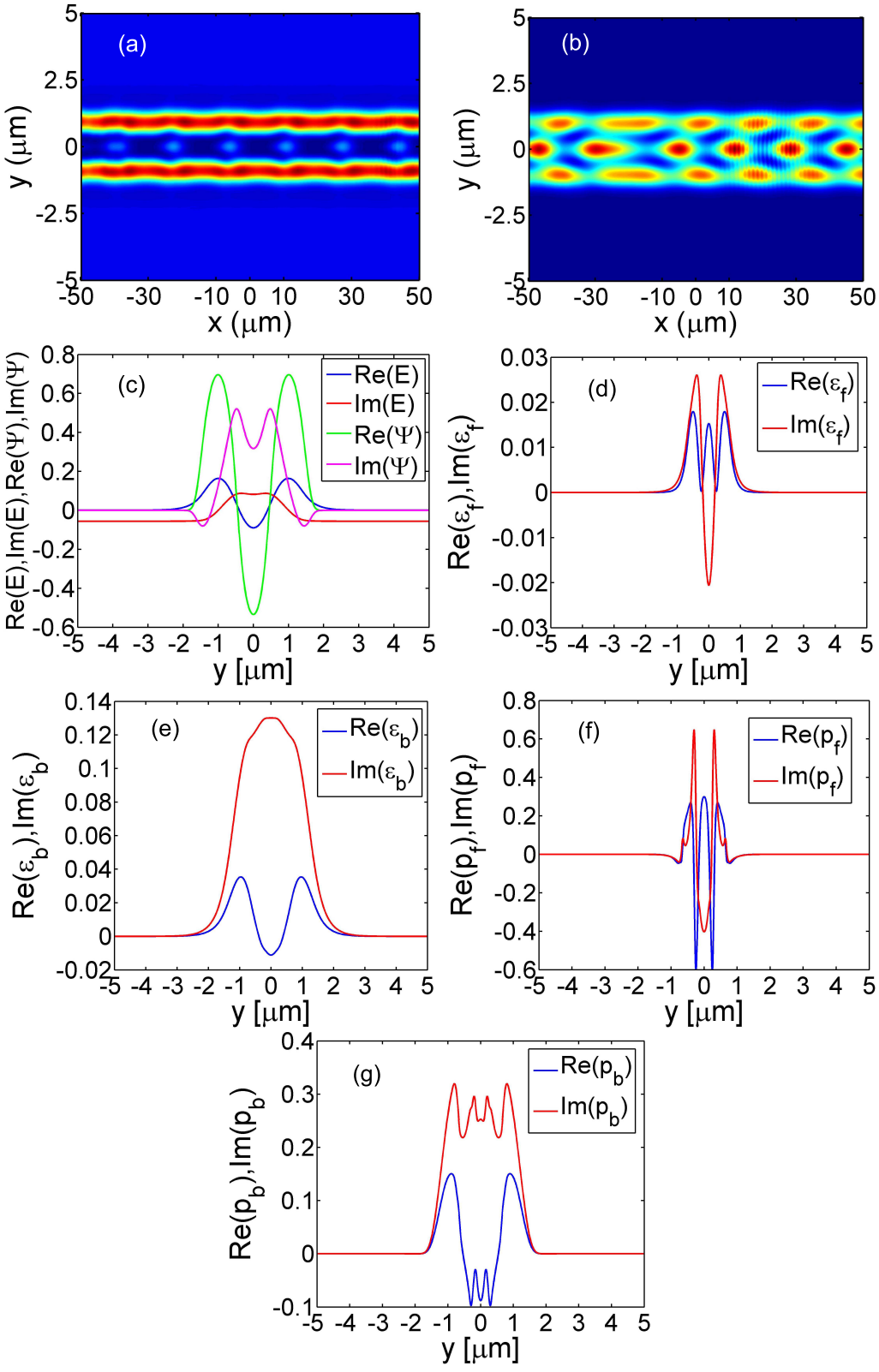

Figure 6: (Color online) Dynamical check of the modulational instability of the stationary solution: snapshots of the time evolution of the perturbed mode at pump amplitude $E_p = 0.087$ and perturbation wave vector $q = 0.2$ (corresponding to the second branch in Fig. 4 (a), and Fig. 3 (b)) at (a) $t = 0.4\,\mathrm{ps}$ and (b) $t = 28.4\,\mathrm{ps}$. Perturbation of the mode on the second branch clearly leads to filamentation, rather than localisation. (c) Real and imaginary parts of the nonlinear polariton mode of the photon (E) and exciton (Ψ) for $E_p = 0.087$, which is on the second branch. (d–g) Real and imaginary parts of the perturbation eigenvectors, computed from Eq. 7.

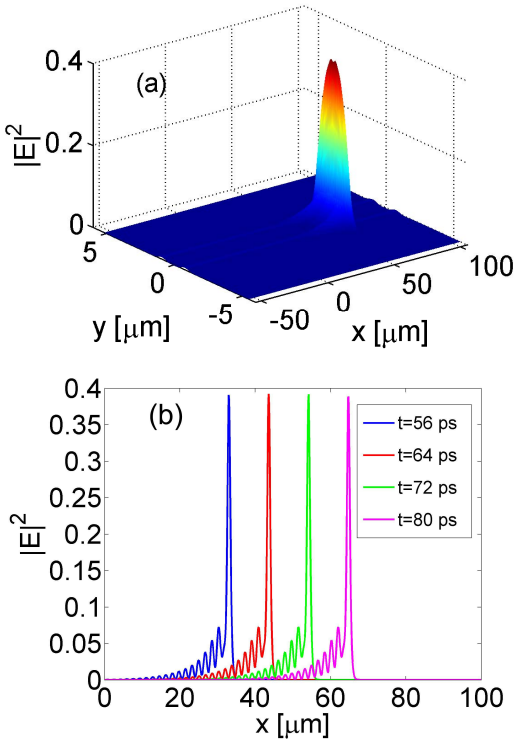

Figure 7: (Color online) Snapshot at $t = 80\,\mathrm{ps}$ of the electric-field intensity of a single-soliton solution at $\Delta = 0$ and $\gamma = 0.04$ for pump amplitude $Ep = 0.075$ and seed pulse duration $\tau = 2\,\mathrm{ps}$. (b) Cross-section of the above along the middle of the microcavity wire (i.e. at $y = 0$), showing the intensity profile of the soliton at four different time points: $t = 56, 64, 72$ and $80\,\mathrm{ps}$.

3.4 Dynamical modelling of soliton formation

We choose the pump amplitude within the interval of existence of solitons (see Fig. 4 (a), shaded area) and initialise the system with the stable mode from the lowest branch. The soliton formation is triggered at time $t = 0$ by a short ($\tau = 2\,\mathrm{ps}$) Gaussian seed pulse with intensity FWHM of $3\ \mu\mathrm{m}$. The pulse is collinear with the pump and provides perturbation to the stationary solution. We solve the system of equations, Eq.(1–1), in the time domain by the split-step method. Following a transient process of initial pulse reshaping (data not shown), a soliton is formed. The stable soliton solution at $\Delta = 0$ and $\gamma = 0.04$ is displayed in Fig. 7 (a) for $E_p = 0.075$. Cross-sections of the soliton profile in (a) through the middle of the microcavity wire ($y = 0$) are shown for different simulation times in Fig. 7 (b). From these it is clear that the soliton shape is preserved during propagation along the wire.

In Fig. 8 (a), a transverse cross-section of the E-field power, $|E|^2$, through the soliton maximum and the stationary nonlinear mode of branch 3 are plotted on the same graph. The soliton maximum is lying above branch 3. In Fig. 8 (b), a transverse cross-section of the E-power in the soliton tail, along with the nonlinear mode corresponding to the lowest branch (branch 1) at $E_p = 0.075$ are shown. The soliton and the nonlinear mode differ in the peak, but do not significantly differ in the tail. The soliton is sitting on the lowest-branch stationary mode and extends above the top branch (branch 3). For $E_p = 0.075$, the soliton temporal width (at FWHM), $T_p = 0.727\,\mathrm{ps}$, is nearly one-half of the soliton temporal width in a planar microcavity ($\sim 1.25\,\mathrm{ps}$) [12], and the soliton is squeezed along the microcavity wire.

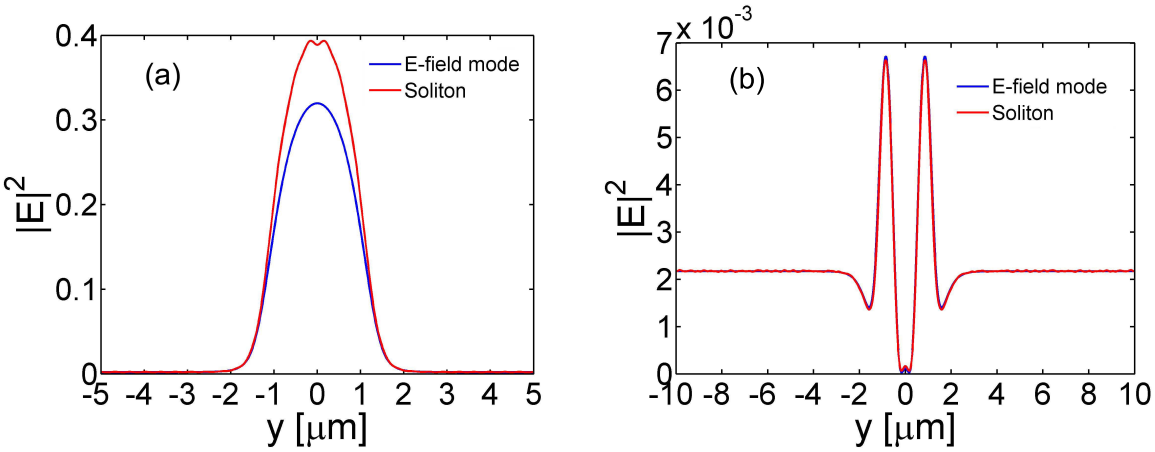

Figure 8: (Color online) Transverse cross-section through: (a) the soliton maximum (red curve) and the stationary mode (blue curve) on branch 3 of the multistability curve (see Fig. 4 (a)); (b) the soliton tail (red curve) and the stationary mode (blue curve) on branch 1. $w = 3\mu m$, $\theta = 20°$, $E_p = 0.075$, $\Delta = 0$, and $\gamma = 0.04$.

3.5 Radiating soliton: collapses and revivals

In this section, we study multistability and soliton formation in a microcavity wire with the same width and incidence angle as before (i.e. $w = 3\,\mu\mathrm{m}$, $\theta = 20°$ and $\Delta = 0$) but this time with lower dissipation, $\gamma = 0.01$. These conditions correspond to the multistability curve denoted by the red dashed line in Fig. 2 (d).

The multistability curves for the E-field and Ψ-field integrated mode powers, obtained from Eqs. 4, are shown in Fig. 9 (a) and (b). We performed a linear stability analysis, and the sections of the curve corresponding to stable, modulationally unstable and unstable nonlinear homogeneous solutions have been identified. However, in this case we could not find solitons of the type that we found for the former case of $\gamma = 0.04$. Instead, we found an interesting type of radiating soliton in the vicinity of $E_p = 0.0341$, which recovers after emitting radiation.

The time evolution of this radiating soliton is displayed in Fig. 9 (c). The resonant radiation, manifested in the appearance of a second peak in the trailing edge of the pulse, is likely due to higher-order dispersion effects, and leads to pulse damping. As a result, the soliton dynamics is described by periodic collapses upon radiation, followed by revivals. After a pulse break-up and emission, the soliton is recovered (see pulse profiles at 110 and 125 ps in Fig. 9 (c)). Similar to semiclassical Rabi oscillations, the soliton excitation and decay at this pump amplitude completes a full cycle. This curious interference phenomenon is reminiscent of the collapses and revivals of resonant coherent pulses propagating in and interacting with a resonantly absorbing/amplifying medium which, on the condition that the pulse duration is smaller than the relaxation times in matter, results in a polariton soliton whose pulse area is conserved during propagation (owing to the Pulse Area Theorem [17]). In this case, the Pulse Area Theorem is indeed satisfied, since $\gamma = 0.01$ corresponds to a relaxation time $T(= T_1 = T_2) \sim 12\,\mathrm{ps}$, which is greater than the pulse duration (2 ps).

The observed periodic dynamics is strongly dependent on the initial conditions, and in particular on the pump amplitude. Only excitations in a very narrow interval around the pump amplitude (approximately $[0.025, 0.035]$ from our simulations) result in this peculiar dynamics. The revivals and collapses take place at regular intervals. An estimate for the time interval between soliton collapses, t_c, can be derived

from comparing the first and the last frames in Fig. 9 (c), giving $t_c \sim 10$–15 ps.

It should be noted that the above analogy with Rabi oscillation collapses and revivals is incomplete, since the revival component of the phenomenon cannot be explained classically (i.e., without introducing photon field quantisation) [18]. The semiclassical Gross-Pitaevskii mean-field model we have presented in this paper could only explain destructive interference effects, such as pulse collapses. We find numerically that the interplay of the multiple discrete nonlinear modes within the microcavity wire results in a semiclassical coherent effect, mimicking the quantum dynamics of collapses and revivals. This interesting coherent propagation phenomenon deserves further investigation and should be a subject of future studies.

3.6 Impact of wire width on the linear polariton energy and mode group velocity dispersion

In this section, we investigate the dependence of the linear free polariton modes dispersion on the channel width. The linear energy dispersion, $\omega(\kappa)$, of the fundamental mode is shown in Fig. 10 (a) for different microcavity widths. Similar to Fig. 1 (b), the dispersion becomes steeper with increasing wire width. In agreement with this trend, the group velocity (Fig. 10 (b), being the slope of the energy dispersion curves at each point) monotonously increases with increasing wire width. The upper bound is the group velocity corresponding to a single-mode planar microcavity.

Let us compare first the soliton velocity at a channel width $w = 3\,\mu\mathrm{m}$ with the one for non-interacting polaritons. The group velocity of the fundamental free polariton mode is calculated as the slope of the fundamental mode linear dispersion curve at pump wave vector $\kappa/L = 2.6862\,\mu\mathrm{m}^{-1}$, corresponding to an angle of incidence $\theta = 20^\circ$. This gives $v_g^{(0)} \approx 1.472\,\mu\mathrm{m/ps}$. The group velocity is very similar to the soliton velocity calculated by the 2D Newton-Raphson method for $E_p = 0.075$, which gives $v_{g,sol} \approx 1.3\,\mu\mathrm{m/ps}$, as well as with the one that can be inferred from the dynamical simulation through comparing consecutive time frames, which is $v_g^{(0)} \approx 1.1875\,\mu\mathrm{m/ps}$. The free polariton group velocity monotonically decreases with the mode number (see slopes for lower polariton branch in Fig. 1 (b)). At this pump wave vector ($\kappa/L = 2.6862\,\mu\mathrm{m}^{-1}$), the first-order mode group velocity is $v_g^{(1)} = 0.96\,\mu\mathrm{m/ps}$; for the second-order mode, $v_g^{(2)} = 0.549\,\mu\mathrm{m/ps}$, or nearly a third of the soliton velocity. For the 3rd and 4th-order modes, it decreases even further: $v_g^{(3)} = 0.313\,\mu\mathrm{m/ps}$ and $v_g^{(4)} = 0.227\,\mu\mathrm{m/ps}$, respectively.

We find that the soliton group velocity obtainable with this microcavity wire geometry (Fig. 1 (a)) is always lower than that of a soliton propagating in a single-mode microcavity $(\sim 1.68\ \mu\mathrm{m/ps})$ [12].

3.7 Soliton branches at different channel widths

The soliton branches computed by the 2D Newton method for different channel widths are shown in Fig. 11. From inspection of Fig.11 (a),(c),(e), as well as data we have not shown, the interval of soliton existence is largest for channel widths in the interval $w \in [2.5, 2.81]\,\mu\mathrm{m}$. The soliton splits into two solitons at the bifurcation point that occurs in the vicinity of $w = 2.86\ \mu\mathrm{m}$, Fig. 11 (c). This point corresponds to the appearance of a middle bistability branch (see arrow in Fig. 11 (d)), or equivalently, a second bistability loop. Upon increasing the wire width beyond $w = 4.8\ \mu\mathrm{m}$, the multistability curve acquires an extra (third) bistability loop (Fig. 11 (f), curve in magenta). However, note that we found no solitons for $w = 6\,\mu\mathrm{m}$ (the 2D Newton-Raphson method did not converge).

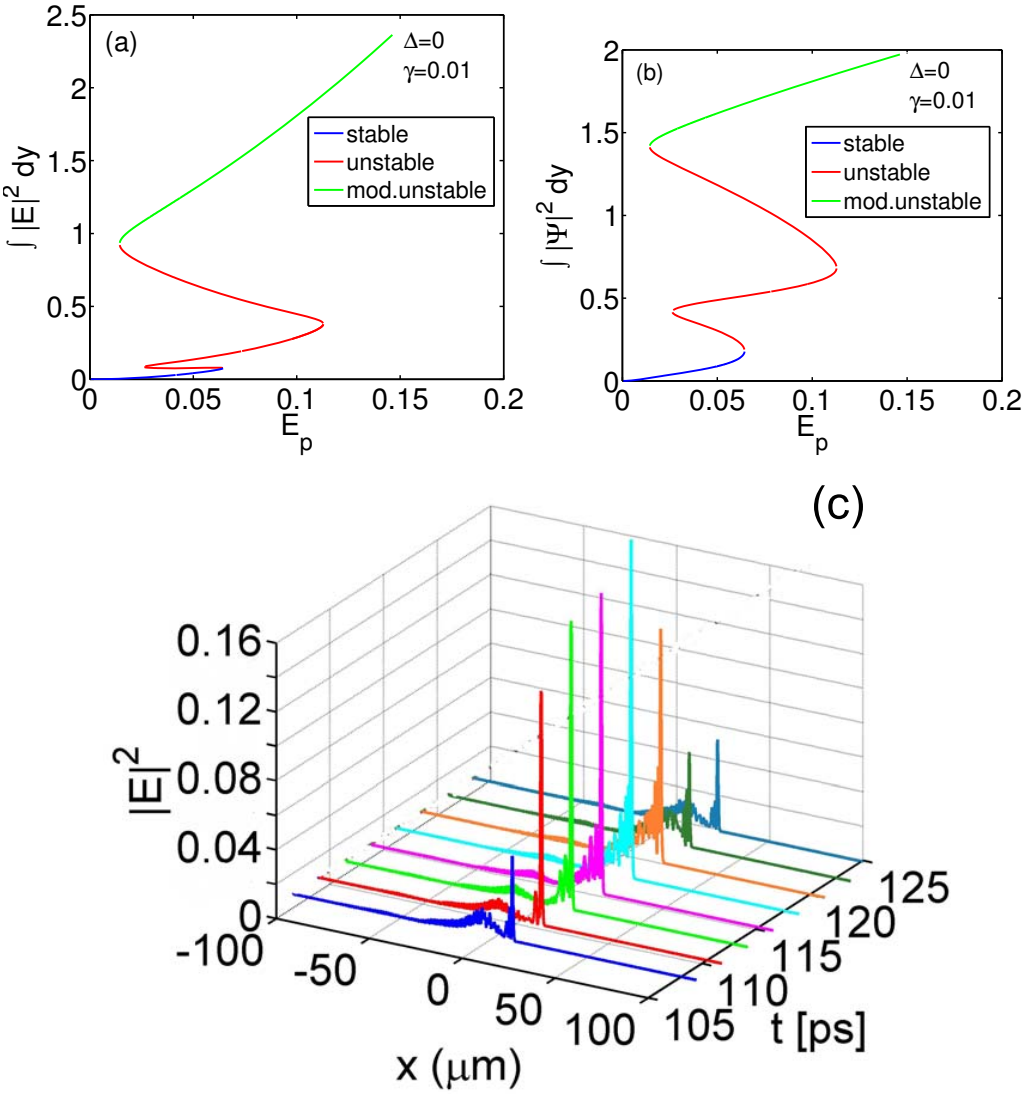

Figure 9: (Color online) Integrated electric-field intensity of the (a) photon (E) and (b) exciton (Ψ), and its dependence on the pump amplitude, E_p, for $\Delta = 0$ and $\gamma = 0.01$. Two bistability loops are exhibited. Sections of the multistability curve containing stable solutions are depicted in blue; unstable – in red, and modulationally unstable – in green. (c) Time evolution of the radiating soliton propagating along the microcavity wire. Snapshots of the E-field intensity profile along the middle of the wire (i.e., along the x axis) at $t = 108, 110.4, 112.8, 115.2, 117.6, 120, 122.4$, and $124.8\,\mathrm{ps}$. In this case, $E_p = 0.0341$. Radiating solitons are observed only over a very narrow interval of pump amplitudes, which is approximately $[0.025, 0.035]$.

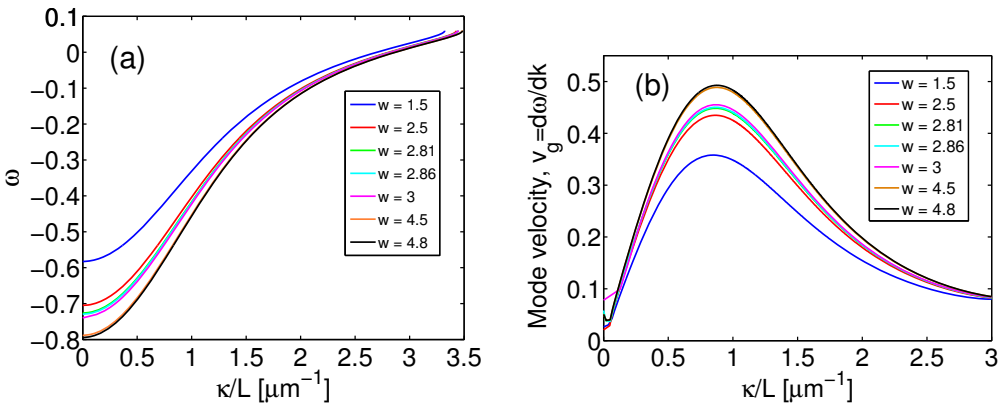

Figure 10: (Color online) (a) Linear fundamental polariton mode dispersion, $\omega(\kappa)$, in dimensionless units for a range of waveguide widths between $1.5\ \mu\mathrm{m}$ and $4.8\ \mu\mathrm{m}$; (b) Fundamental mode group velocity dispersion for the same range of waveguide widths as in (a).

The group velocity and the maximum amplitude of the soliton as a function of wire width are shown in Fig. 12. Our model predicts a non-monotonous behaviour of both quantities. From Fig. 12 (a), it is clear that the slowest soliton is obtained for the narrowest wire. However, we observe further local maxima and minima in the curve. Here we will attempt to give a qualitative explanation of the non-monotonous behaviour we have predicted.

Starting with $w = 1.5\,\mu\mathrm{m}$, as the width is increased, the soliton group velocity increases, reaching a maximum at $w = 2.81\,\mu\mathrm{m}$. At this point, we speculate that a second-order mode appears, whose group velocity is much lower than that of the fundamental mode (about $2/3$ reduction in velocity; see end of Sec. 3.6). This results in a decrease of the overall soliton group velocity. The soliton can then be viewed as a composite multi-mode entity, consisting of a fundamental and second-order modes. Further increase of the wire width leads to the bifurcation point at $w = 2.86\ \mu\mathrm{m}$ in Fig. 11 (c), where we suppose the fourth-order mode appears. With a group velocity $1/6$th of the fundamental mode group velocity, the fourth-order mode therefore decreases the composite soliton group velocity even further, which reaches a minimum at $w = 3\ \mu\mathrm{m}$. When the wire width is increased beyond this point, the soliton group velocity increases, as its constituent mode group velocities increase with wire width. This continues until another maximum is reached at around $w = 4.4\ \mu\mathrm{m}$. Beyond this point, we expect that a sixth-order mode appears, and the soliton velocity drops again. Following this line of reasoning, we would expect to encounter another bifurcation just below $w = 6\ \mu\mathrm{m}$, where a third bistability loop appears (see curve in magenta in Fig. 11 (f)). We expect that the soliton group velocity drops to zero at $w = 6\ \mu\mathrm{m}$, since we were not able to find a soliton for this wire width.

The dependence of the maximum soliton amplitude on the wire width is shown in Fig. 12 (b). It is very similar to the soliton group velocity non-monotonous dependence, which indicates a correlation between the two. Although at this stage we cannot comment on the origin of this, it would be interesting to investigate the nature of this relationship in the future.

In order to explain quantitatively this peculiar non-monotonous behaviour, we have recently developed a coupled-mode expansion method [16]. Detailed analysis using this method will be presented in a forthcoming paper.

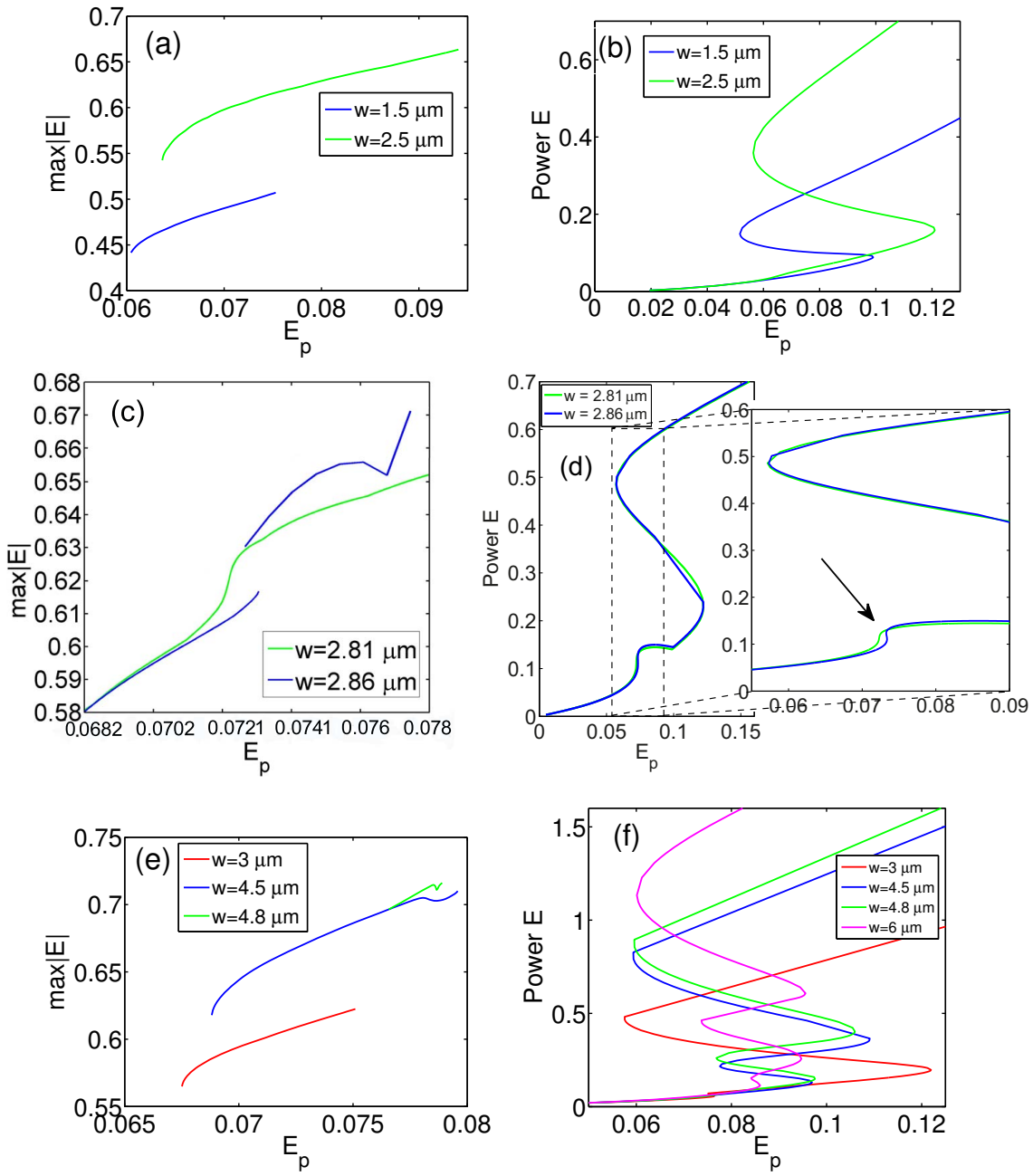

Figure 11: (Color online). (a) Soliton branches, plotted as the maximum of the modulus of the soliton's photon electric field (E) against the pump amplitude, E_p. This was computed by the 2D Newton-Raphson method. (b) Integrated E-field power (i.e., $\int |E|^2 dy$) bistability curves for channel widths $w = 1.5$ and $2.5\,\mu$m. (c) Soliton branches and (d) E-field power bistability curves in for $w = 2.81$ and $2.86\,\mu$m, in the vicinity of a bifurcation point. Soliton existence for the widest range of pump amplitudes is achieved in interval $w \in [2.5, 2.81]\,\mu$m, where the bistability curve gains another loop (arrow). (e) Soliton branches and (f) E-field power multistability curves for $w = 3, 4.5, 4.8$ and $6\,\mu$m. The multistability curve at $w = 6\,\mu$m exhibits 3 loops (and 3 folding points); however, at this channel width, no soliton was found using the 2D Newton-Raphson method. For all panels in this figure, pump detuning, $\Delta = 0$ and cavity decay rate, $\gamma = 0.04$.

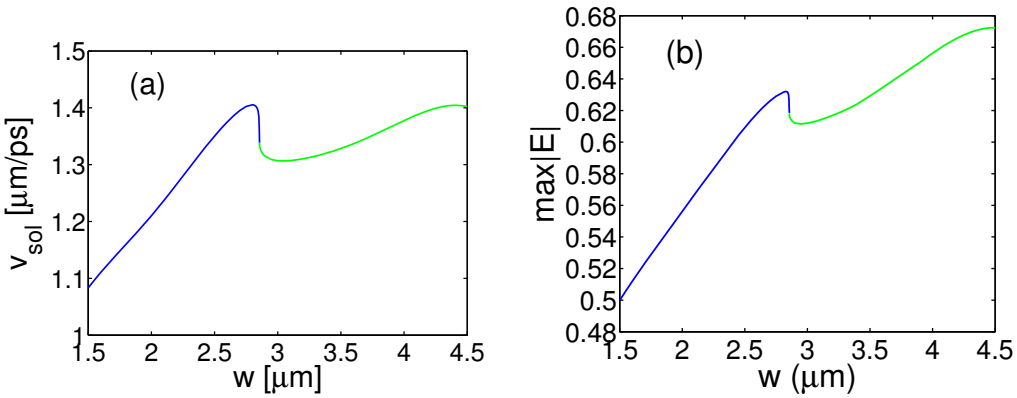

Figure 12: (Color online) (a) Soliton group velocity and (b) maximum soliton amplitude as a function of wire width at $\Delta = 0, \gamma = 0.04$. These results were computed with the 2D Newton-Raphson method. The point where the colour of the curve changes ($w = 2.86\ \mu\mathrm{m}$) corresponds to a bifurcation point in the multistability curve.

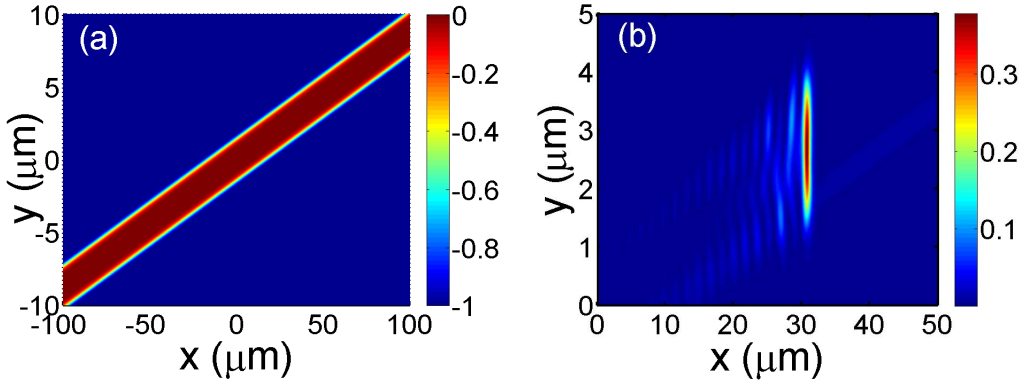

Figure 13: (Color online) (a) Top view of the 3D potential, $U(y)$ (see Eqs. (2)), of a microcavity wire tilted at an angle $\alpha = 5^\circ$ with respect to the x axis. (b) An expanded top view of a single frame at $t = 24\,\mathrm{ps}$ of a soliton (pump amplitude $E_p = 0.075$, seed amplitude $E_s = 0.5$) propagating in the tilted microcavity wire. The squared modulus of the electric field of the photon constituent of the polariton soliton, $|E|^2$, is plotted.

3.8 Soliton propagation in tilted microcavity wires

We have performed a number of dynamical simulations with wires oriented at different tilt angles with respect to the x axis for $\Delta = 0$ and $\gamma = 0.04$. In Fig. 13 (a), a microcavity wire tilted at an angle $\alpha = 5^\circ$ is shown for a wire width $w = 3\,\mu\mathrm{m}$, pump angle of incidence $\theta = 20^\circ$ and pump amplitude $E_p = 0.075$. We trigger the polariton soliton formation with a seed pulse, as described in the beginning of Sec. 3.4. Following brief initial reshaping, the soliton travels undistorted along the tilted microcavity wire (Fig. 13 (b) and video in [**?**]). For $E_p = 0.075$, we found that the soliton is preserved in amplitude up to tilt angles $\alpha \sim 6^\circ$. Larger tilt angles, however, lead to destruction of the soliton. Our dynamical results above were checked by 2D Newton-Raphson method calculations. Using the latter method, the dependence of the soliton E-field maxima on the microcavity wire tilt angle is plotted for different pump amplitudes in Fig. 14 (a). The dependence is nonlinear and exhibits typical critical behaviour; the soliton disappears at different critical angles for different pump amplitudes. The critical

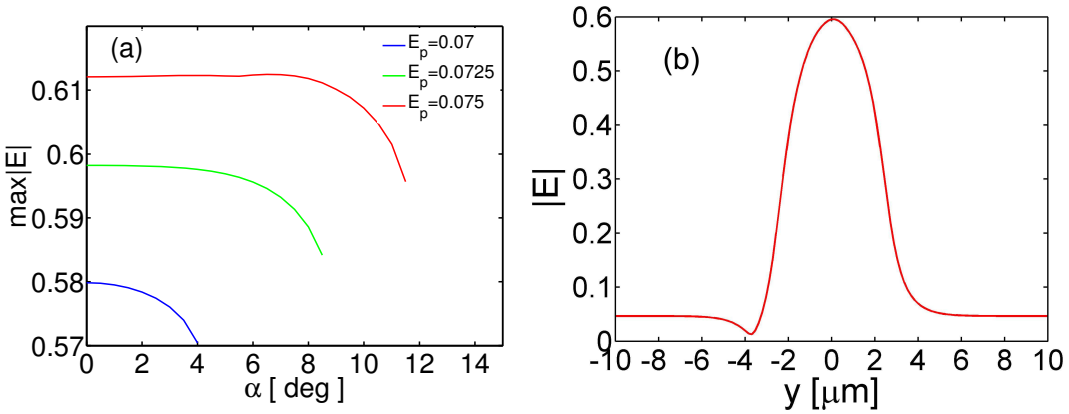

Figure 14: (Color online) (a) Maximum of modulus of the electric field (E) of the photon part of the soliton, as a function of tilt angle, α, shown for three different pump amplitudes. The soliton persists with relatively constant amplitude up to a maximum tilt angle of $\alpha = 8^\circ$ for $E_p = 0.075$. (b) Transverse cross-section through the soliton at $E_p = 0.075$ for $\alpha = 8^\circ$, the maximum tilt angle for which the soliton is preserved in amplitude. Note that the soliton profile is asymmetric.

angle monotonically increases with increasing pump amplitude, reaching a maximum of $\alpha_{max} \sim 12^\circ$ at pump amplitude $E_p = 0.075$. The amplitude remains unchanged up to 8°. In fact, the soliton can persist up to almost 12°, albeit with a small loss in amplitude (about 2.5%). The transverse cross-section through the soliton maximum, calculated by the 2D Newton method at $\alpha = 8^\circ$ and $E_p = 0.075$, is shown in Fig. 14 (b). The soliton exhibits a pronounced asymmetric shape. The maximum critical angle obtained by the 2D Newton-Raphson method differs by ~ 2 degrees from the one calculated by the time-dependent split-step method. This is a very good agreement, giving an indication of the microcavity wire tilt limitations in designing soliton polaritonic splitters, routers and other functional components of future polaritonic integrated circuits.

3.9 Soliton propagation in tapered microcavity wires

From Fig. 12, it follows that the soliton amplitude increases with increasing microcavity wire width in the interval $w \in [1.5, 2.81]\,\mu\mathrm{m}$, and $w \in [2.86, 4.5]\,\mu\mathrm{m}$. This effective soliton amplification effect can be exploited in specially designed tapered microcavity wires. In Fig. 15 (a) and (b), the confinement potential of a tapered wire with initial and final widths $w = 1.00\,\mu\mathrm{m}$ and $w = 4.02\,\mu\mathrm{m}$, respectively, is shown. The Rabi frequency potential is constructed in the same way as in the second of Eqs. (2), whereby the coupling is 1 within the channel and zero outside (data not shown).

A soliton is launched from the left boundary. The time evolution of the soliton power, $|E|^2$, is shown in Fig. 15 (c) and (d), for two simulation times, $t = 48$ and 120 ps near the beginning and end of the wire. As the soliton traverses the structure, it expands in the y direction, but holds together along x and does not dissipate. Snapshots of the time evolution of the soliton during propagation along the tapered wire are shown in Fig. 15 (e). The first (leftmost) profile shown is at a point near the left boundary, where the soliton is being excited by the seed pulse. After some initial reshaping, a soliton is formed. Due to the smooth change in width of the wire, the soliton power increases adiabatically, reaching maximum at wire width $w \approx 2.44\mu\mathrm{m}$ (Fig. 15 (e)). Subsequently, the power drops down sharply, reaching a minimum at $w \approx 2.7\mu\mathrm{m}$, whereupon it gradually increases again. As we shall show below, this non-monotonic behaviour is in very good quantitative agreement with the calculated

by the 2D Newton-Raphson method dependence of the power on the wire width.

In Fig. 16 dynamically simulated excitation and propagation of a soliton in a tapered wire with initial and final widths: $w \sim 1\,\mu\mathrm{m}$ and $w \sim 4\,\mu\mathrm{m}$, respectively, at a pump amplitude $E_p = 0.075$ is shown (in red) along with the width dependence of the maximum soliton amplitude, as computed by 2D Newton-Raphson method (see Fig. 12(b)) are plotted. Following initial reshaping (see initial portion of the red curve) the soliton reaches a maximum at a lower wire width than $2.81\,\mu\mathrm{m}$ (blue curve), after which the curve decreases, going through an inflexion point (bifurcation), reaches a minimum and continues to increase, reaching another maximum. Note that this behaviour is exactly of the type of non-monotonic behaviour of the 2D Newton-Raphson curve in Fig. 12(b), and the maximum soliton amplitudes computed by the two methods are in a very good agreement. The shift along w-axis is due to the soliton being excited dynamically at a point along the wire ($w < 1.5\ \mu\mathrm{m}$), preceding the first calculated point by 2D Newton-Raphson. Therefore, the maximum of the curve is reached earlier and the overall curve is translated to the left. For the selected pump amplitude of $E_p = 0.075$ there is no soliton at $w = 4.8\ \mu\mathrm{m}$, despite the computed branch in Fig. 11(e) - green curve, because there is no pump amplitude that is shared between all branches.This is the reason why the maximum soliton amplitude width dependence in Fig. 12(b) does not continue beyond the final point, corresponding to $w = 4.5\ \mu\mathrm{m}$.

The soliton FWHM for the same tapered microcavity wire is plotted in Fig. 16 (b). After the transient soliton formation process at the end of which a minimum FWHM is reached, the soliton FWHM monotonically increases by $\sim 30\%$.

4 Conclusions

We have developed a model of the polariton nonlinear dynamics in non-planar microcavity wires, based on driven-dissipative 2D mean-field Gross-Pitaevskii coupled equations.

For a realistic microcavity wire structure, we found that the conventional bistability of the nonlinear mode power upon variation of the pump amplitude, typical for planar microcavities, evolves into complex multistability in microcavity wires that can be linked to the composite multi-mode structure of the branches in the multistability curve. We have discussed the origin of the multistability in detail and traced it back to the spatial symmetry of the pump and the pump frequency detuning from the frequencies of the confined microcavity wire modes (the number of confined modes being dependent on the microcavity wire confinement potential depth and width). The pump imposes its symmetry on the nearest modes in the frequency domain, resulting in suppression of the odd modes and survival of the nearest even modes only.

Employing linear stability analysis and conducting dynamical simulations we have discovered a range of pump amplitudes, for which polariton solitons exist in a realistic structure in the triggered parametric oscillator regime. We have confirmed these results by the 2D Newton-Raphson method. In contrast to the single-mode polariton solitons in planar microcavities, polariton solitons obtained by our scalar model in microcavity wires exhibit a complex multi-mode structure. This type of spatially localised polariton solitons deserve special attention, and we have developed a modal expansion method [16] to investigate the inter-modal nonlinear interactions and mechanisms of localisation, as well as to provide leverage to exercise control over the multimode interactions and polariton dynamics.

We have investigated the possibility of exciting solitons with lower dissipation (when the exciton and cavity decay rates are lower) in view of recent advances in fabrication of microcavities with ultrahigh polariton lifetimes [7, 8]. We numerically demonstrated a special type of radiating polariton soliton,

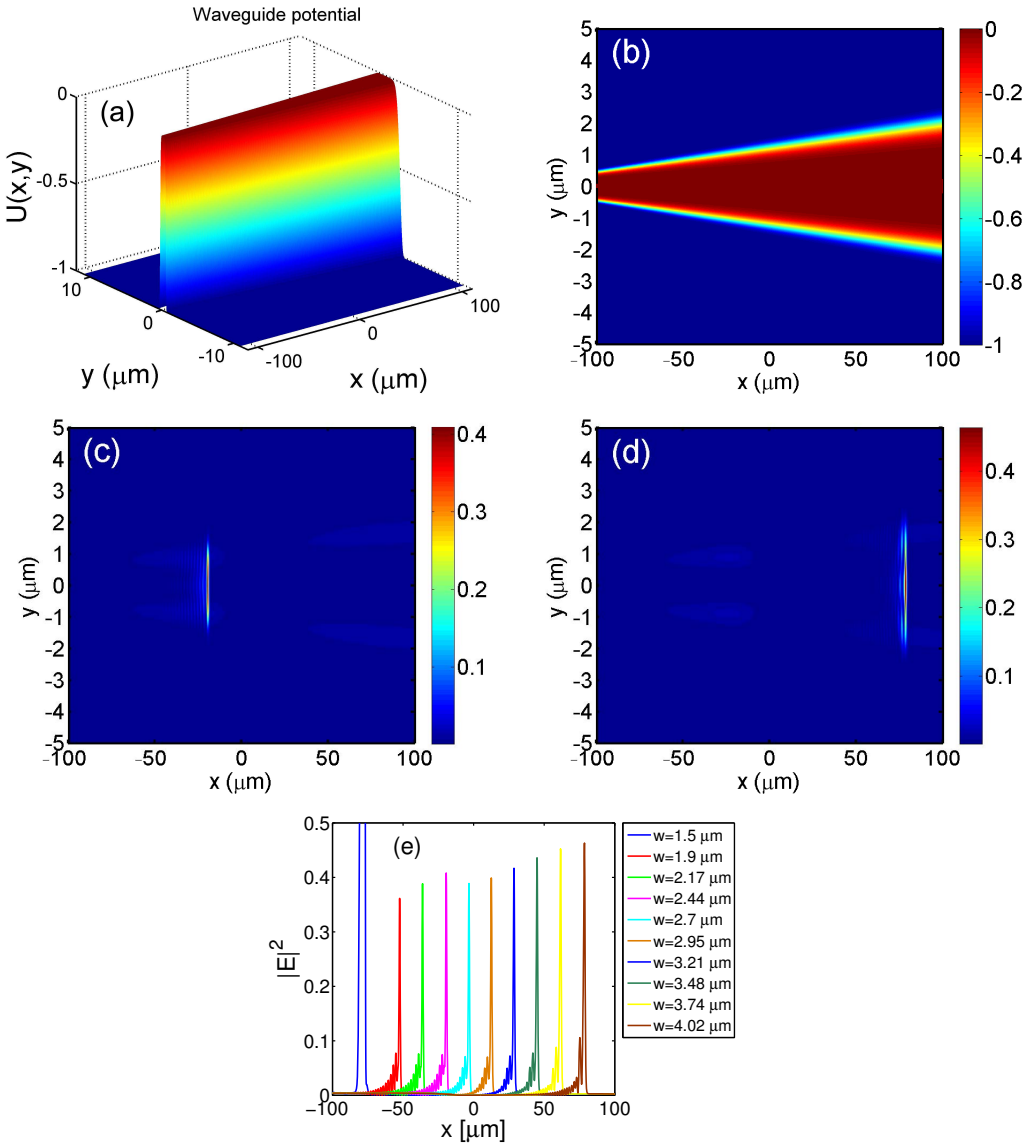

Figure 15: (Color online) (a) 3D confinement potential of a tapered microcavity wire, with input facet width, $w = 1.00\,\mu\mathrm{m}$, and output facet width, $w = 4.02\,\mu\mathrm{m}$. (b) Top view of the potential. (c) and (d): time evolution of a soliton propagating in the tapered microcavity. Modulus squared of the electric field of the photon part of the soliton, $|E|^2$, at (c) $t = 48\,\mathrm{ps}$ and (d) $t = 120\,\mathrm{ps}$, showing that, as it travels, the soliton broadens in the y direction but remains focused in the x. (e) Profiles of the polariton soliton at different moments in time: $t = 2.4, 24, 36, 48, 60, 72, 84, 96, 108$ and 120 ps, corresponding to tapered microcavity wire widths: $w = 1.5, 1.9, 2.17, 2.44.2.7, 2.95, 3.21, 3.48, 3.74$ and $4.02\,\mu\mathrm{m}$. The soliton amplitude adiabatically increases, peaks around the bifurcation point, then subsequently decreases, reaching a minimum, after which it increases again (see Fig. 12 (b) and Fig. 11 (c)).

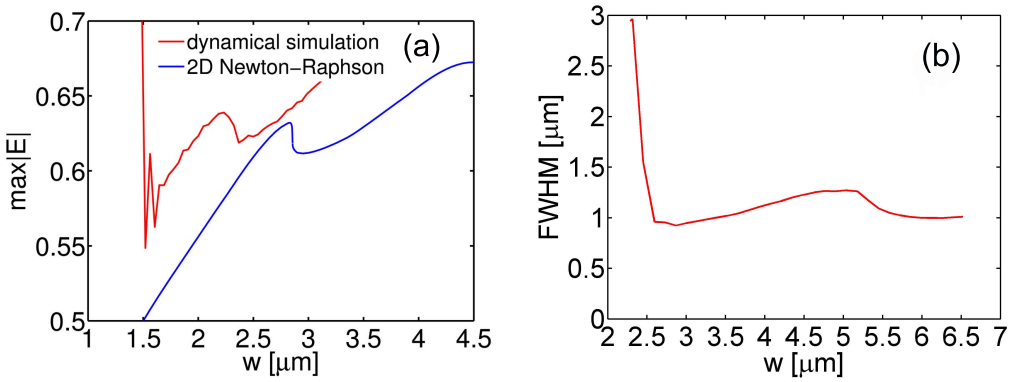

Figure 16: (Color online) (a) Dynamical simulation of the soliton excitation and propagation in a tapered microcavity wire ($E_p = 0.075$) along with 2D Newton-Raphson method calculated dependence of the maximum soliton amplitide on the microcavity wire width (blue curve) from Fig. 14(b). The dynamically calculated maximum soliton amplitude (red curve) has the same type non-monotonic dependence on w as the one calculated by Newton-Raphson method (blue curve), however is shifted to the left along w-axis, which is due to the excitation of a soliton at a point near the left boundary, before the first calculated point by 2D Newton-Raphson (at $w = 1.5\ \mu\mathrm{m}$). Note also that initial soliton reshaping (the first points on the red curve) takes place before a stable soliton is formed; (b) Soliton FWHM vs wire width for the same tapered wire as in (a) the soliton FWHM decreases reaching a minimum at $w \sim 2.5\ \mu\mathrm{m}$ and subsequently increases by $\sim 30\%$.

exhibiting collapses and revivals during propagation along the microcavity wire. In view of device applications, we have studied dynamically polariton soliton propagation in a tilted microcavity wire, and identified critical tilt angles above which the solitons vanish. The latter are in very good agreement with 2D Newton-Raphson calculations. In the tapered microcavity wire, we found that the polariton soliton maximum amplitude increases for certain microcavity wire widths, which allows to design solitons with specific characteristics, or to exploit the soliton amplification effect. One can envisage the use of tapered microcvavity wire sections in an integrated device as means for reshaping and amplifying the polariton solitons. For instance, tapered sections can be used for boosting the soliton amplitude which could act as repeaters on a transmission line, compensating loss at junctions. Furthermore, the complex dependence of the soliton group velocity on the wire width effectively means that the latter can be optimised according to whether fast or slow polariton solitons are required for a particular device application. For instance, fast polariton solitons are necessary for ultrafast polariton switches and modulators with applications in quantum information technologies, e.g. routing entangled single photons. Conversely, similar to the slow-light effect [19], designing geometries supporting slow polariton solitons should leat to an enhancement of the nonlinear response, thereby decreasing the threshold for nonlinear effects, such as polariton parametric scattering and Kerr effect. These slow polariton solitons may have applications as controllable delay lines and buffers. Clearly these studies are of great importance for physical realisation of low-consumption, low-intensity threshold polariton integrated circuits.

In summary, this work lays the foundations for simulation of basic building blocks of the future polaritonic integrated circuits, such as X- and Y-splitters, couplers and routers, based on soliton logic.

References

References

[1] D. W. Snoke, in *Exciton Polaritons in Microcavities*, Eds. V Timofeev and D. Sanvitto, Springer Series in Solid State Sciences, **172** (Springer, New York, 2011)

[2] C. Ciuti, P. Schwendimann, B. Deveaud, and A. Quattropani, *Theory of the angle-resonant polariton amplifier*, Phys. Rev. B **62**, R4825–R4828 (2000)

[3] D. M. Whittaker, *Classical treatment of parametric processes in a strong-coupling planar microcavity*, Phys. Rev. B **63**, 193305-1 – 193305-1(2001)

[4] N.H. Kwong, R. Takayama, I. Rumyantsev, M. J. Kuwata-Gonokami, and R. Binder, *Third-order exciton-correlation and nonlinear cavity-polariton effects in semiconductor microcavities*, Phys. Rev. B **64**, 045316 (2001)

[5] A. Amo, D. Sanvitto, F. P. Laussy, D. Ballarini, E. del Valle, M. D. Martin, A. Lemaître, J. Bloch, D. N. Krizhanovskii, M. S. Skolnick, C. Tejedor, and L. Viña, *Collective fluid dynamics of a polariton condensate in a semiconductor microcavity*, Nature **457**, 291–296 (2009)

[6] A. Amo, S. Pigeon, D. Sanvitto, V. G. Sala, R. Hivet, I. Carusotto, F. Pisanello, G. Leménager, R. Houdré, E Giacobino, C. Ciuti, A. Bramati, *Polariton Superfluids Reveal Quantum Hydrodynamic Solitons*, Science **332**, 1167 – 1169 (2011)

[7] B. Nelsen, G. Liu, M. Steger, D. W. Snoke, R. Ballili, K. West, and L. Pfeiffer, Phys. Rev. X **3**, 041015 (2013)

[8] M. Steger, G. Liu, B. Nelsen, C. Gautham, D. W. Snoke, R. Ballili, L. Pfeiffer, and K. West, Phys. Rev. B **88**, 235314 (2013)

[9] M. Steger, C. Gautham, D. W. Snoke, L. Pfeffer, and K. West, Optica **2**, 1 (2015)

[10] H. Deng, H. Haug, and Y. Yamamoto, *Exciton-polariton Bose-Einstein Condensation*, Rev. Mod. Phys. **82**, 1489 (2010)

[11] O. A. Egorov, D.V. Skryabin, A.V. Yulin, and F. Lederer, Bright Cavity Polariton Soliton, Phys. Rev. Lett. **102**, 153904-1–153904-4 (2009)

[12] M. Sich, D. N. Krizhanovskii, M. S. Skolnick, A. V. Gorbach, R. Hartley, D. V. Skryabin, E. A. Cerda-Méndez, K. Biermann, R. Hey and P. V. Santos, *Observation of bright polariton solitons in a semiconductor cavity*, Nature Photonics, **6**, 50–55 (2012)

[13] E. Wertz, L. Ferrier, D. D. Solnyshkov, P. Senellart, D. Bajoni et al., *Spontaneous formation of a polariton condensate in a planar GaAs microcavity*, Appl. Phys. Lett., **95**, 051108-1–051108-3 (2009)

[14] E. Wertz, L. Ferrier, D. D. Solnyshkov, R. Johne, D. Sanvitto, A. Lemaître, I. Sagnes, R. Grousson, A. V. Kavokin, P. Senellart, G. Malpuech and J. Bloch, *Spontaneous formation and optical manipulation of extended polariton condensates*, Nature Physics, **6**, 860–864 (2010)

[15] G. Slavcheva, A. V. Gorbach, A. Pimenov, A. G. Vladimirov and D. V. Skryabin, Opt. Lett. **40**, 1787 (2015)

[16] G. Slavcheva, A. V. Gorbach, and A. Pimenov, Phys. Rev. B **94**, 245432 (2016)

[17] S. L. McCall and E. L. Hahn, Phys. Rev. **183**, 457 (1969)

[18] M. O. Scully and M. S. Zubairy, *Quantum Optics*, (Cambridge Univeristy Press, Cambridge, 1997)

[19] P. Colman, C. Husko, S. Combrie, I. Sagnes, C. W. Wong, and A. De Rossi, Nature Photonics, **4**, 862 (2010)